Journal of
Synchrotron
Radiation

ISSN 1600-5775

Received 16 September 2014
Accepted 7 January 2015

Validation of a *Geant4* model of the X-ray fluorescence microprobe at the Australian Synchrotron

Matthew Richard Dimmock,[a]* Martin Daly de Jonge,[b] Daryl Lloyd Howard,[b] Simon Alexander James,[b] Robin Kirkham,[c] David Maurice Paganin,[d] David John Paterson,[b] Gary Ruben,[c,b] Chris Gregory Ryan[c] and Jeremy Michael Cooney Brown[d]

[a]Department of Medical Imaging and Radiation Sciences, Monash University, Clayton, VIC 3800, Australia, [b]Australian Synchrotron, 800 Blackburn Road, Clayton, VIC 3168, Australia, [c]CSIRO, Clayton, VIC 3168, Australia, and [d]School of Physics and Astronomy, Monash University, VIC 3800, Australia. *E-mail: matthew.dimmock@monash.edu

A *Geant4* Monte Carlo simulation of the X-ray fluorescence microprobe (XFM) end-station at the Australian Synchrotron has been developed. The simulation is required for optimization of the scan configuration and reconstruction algorithms. As part of the simulation process, a Gaussian beam model was developed. Experimental validation of this simulation has tested the efficacy for use of the low-energy physics models in *Geant4* for this synchrotron-based technique. The observed spectral distributions calculated in the 384 pixel Maia detector, positioned in the standard back-scatter configuration, were compared with those obtained from experiments performed at three incident X-ray beam energies: 18.5, 11.0 and 6.8 keV. The reduced χ-squared ($\chi^2_{\rm red}$) was calculated for the scatter and fluorescence regions of the spectra and demonstrates that the simulations successfully reproduce the scatter distributions. Discrepancies were shown to occur in the multiple-scatter tail of the Compton continuum. The model was shown to be particularly sensitive to the impurities present in the beryllium window of the Maia detector and their concentrations were optimized to improve the $\chi^2_{\rm red}$ parameterization in the low-energy fluorescence regions of the spectra.

Keywords: X-ray fluorescence; Gaussian beam; Monte Carlo; simulation; *Geant4*; Maia.

1. Introduction

The X-ray fluorescence microprobe (XFM) beamline at the Australian Synchrotron enables quantitative elemental mapping of a wide range of samples (Lombi *et al.*, 2011; McColl *et al.*, 2012; Howard *et al.*, 2012). The XFM elemental mapping technique primarily involves raster scanning of a sample through a focused X-ray beam at a certain incident monochromatic photon energy and collecting fluorescence spectra at each position in the scan. These spectra can be analysed efficiently to produce maps (typically two-dimensional) of elemental concentration. The use of a rotation stage (de Jonge *et al.*, 2010) or focusing polycapillary (Donner *et al.*, 2012) enables the position dimensionality of the data stack to be increased from two to three. As the size of the parameter space increases and the possibility of volumetric segmentation (de Jonge & Vogt, 2010) is realised, optimization of the scan geometry and reconstruction algorithms becomes increasingly important.

In order to help facilitate scan optimization, a model of the XFM end-station has been developed and validated against experimental data. The model utilizes version 10.0.p01 of the *GEometry ANd Tracking* (Agostinelli *et al.*, 2003; Allison *et al.*, 2006) Monte Carlo software (*Geant4*) to propagate X-rays from the exit of the focusing optics, through the sample and onto the detectors. The measured beam-profile is that of a Gaussian beam. In order that the characteristics of the beam (waist and focal depth) were accounted for, a Hermite–Gaussian beam was incorporated into the simulation. The resulting *Geant4* output data were processed to account for the detector resolution effects before being compared with experimental data. Validation of the model includes data collected at three incident beam energies: E_0 = 18.5, 11.0 and 6.8 keV. The spectra were split into fluor-

escence, elastic and inelastic scatter regions for detailed comparison.

2. Experimental measurements

The XFM beamline utilizes an undulator to produce a horizontally polarized photon beam. A monochromatic energy profile is selected on the downstream double-crystal monochromator (DCM) (Sparks Jr *et al.*, 1980). The beam is then focused by a harmonic rejection mirror onto a secondary source aperture, before traversing an ion chamber where the incident X-ray intensity (I_0) is measured. The X-rays are then refocused by a Kirkpatrick–Baez (KB) mirror pair (Kirkpatrick & Baez, 1948; Yang *et al.*, 1995) where the focal plane is the sample location. Fig. 1(*a*) shows a CAD drawing of the XFM end-station. The beam path is shown by the solid arrow. After exiting the KB mirror pair (K), the beam then passes through the Maia (384A) detector (M) (Kirkham *et al.*, 2010) entrance windows and beam collimator before it intersects the sample on the sample mount (S). Fluorescence emissions resulting from interactions in the sample are collected by the Maia silicon (Si) diode array. Incident X-rays may also interact in the sample and air, and back-scatter into the detector. The sample mount is fixed to an *x*–*y* scanning-stage that allows the specimen to be translated through the beam.

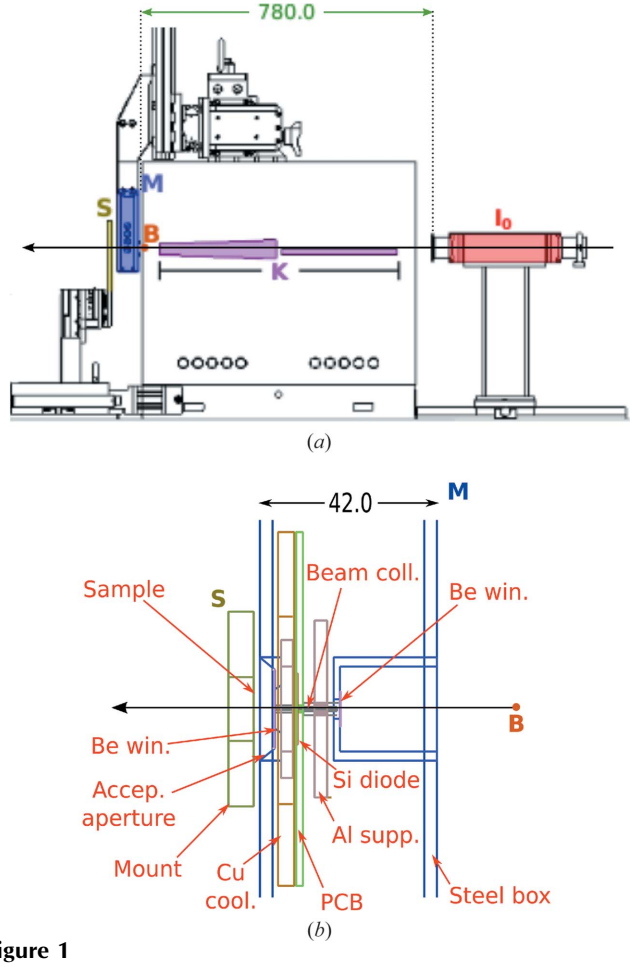

Figure 1
(*a*) CAD drawing of the XFM end-station that shows the beam path (black arrow) traversing the ion chamber (I_0), focusing mirror pair (K), Maia detector box (M) and sample mount (S). (*b*) Side profile of a section of the *Geant4* Monte Carlo model of the XFM end-station, including the Maia detector and sample mount. The length measurements are expressed in mm. The origin of the simulated beam of X-rays is marked as B.

The horizontal and vertical mirrors have focal distances of 0.21 m and 0.43 m and each have an optical aperture of 600 µm. This configuration gives rise to half-angle divergences of 1.43 mrad and 0.70 mrad in the horizontal and vertical directions, respectively.

In a typical mode of operation, the KB mirrors are focused to the sample location [marked as 'Sample' in Fig. 1(*b*)], 51.6 mm from the exit of the mirror pair. The *z*-spacing of the vertical and horizontal mirrors confers different horizontal (*x*) and vertical (*y*) numerical apertures on the beam and produces a focus with an elliptical cross-section. The beam profile can be approximated as being Gaussian (to first order) along each of *x* and *y*, with full width at half-maximum (FWHM) values of 1.5 µm and 1.0 µm, respectively. The depth of focus is approximately 500 µm. Fitting of relative sensitivity data to the solid angle subtended by each detector pixel gave the following for the global tilt angles of the detector relative to the beam: horizontal, −6.9 mrad; vertical, +22 mrad.

X-rays that exit the KB mirror pair and are not removed by collimation subsequently traverse the Maia detector. The Maia detector is comprised of a position- and energy-resolving pixelated Si diode array that is housed in a stainless-steel box. At the centre of this volume is a cylindrical molybdenum (Mo) collimator that shields the active volume of the detector from X-rays that scatter in the beryllium (Be) entrance and exit windows as they traverse the hole in the centre of the detector. The incident beam passes through this collimator before intersecting the sample. The beam collimator intersects an aluminium (Al) support, the detector, a printed circuit board (PCB) and a Mo mask. The detector array is lithographically segmented into 384 pixels. The pixel centres are separated by 1.0 mm in both *x* and *y* on a Cartesian grid. The unimplanted region between pixels is 150 µm, which results in each pixel having an active volume of 0.4 mm × 0.85 mm × 0.85 mm. To minimize the effects of charge-sharing (Mathieson *et al.*, 2002), a Mo mask is fixed to the front surface of the diode. The mask has three layers (Ryan *et al.*, 2010*a*). Each layer is 0.1 mm-thick and has 384 small box volumes and a central hole, to accommodate the beam collimator, cut from it. The areal cross-section of each aperture is calculated such that its size and position collimates X-rays from a target position, at 10 mm, into the active part of each pixel.

Two different types of experimental measurements were collected from the XFM end-station for separate purposes: (i) parameterization of the beam profile and (ii) validation of the Monte Carlo model. These data sets are considered in §2.1 and §2.2, respectively.

2.1. Experimental beam parameterization

In order to ensure that the beam geometry utilized in the simulation was physically motivated, the profile was measured

by stepping a scintillator and charge-coupled device (CCD) camera in unison along the z-axis and through the focal plane. The CCD responses were digitized and fitted. The size of the CCD pixels is 0.35 µm × 0.35 µm.

Fig. 2(a) shows the measured beam intensity profile at the focal plane, z = 51.6 mm (corresponding to z = 19.8 mm on the sample stage). The profile at each location is an elliptical Gaussian to first order. As such, the profile is shown to propagate as a Gaussian beam (see Appendix A). In order to obtain the coefficients of the fit, the measured FWHMs were converted to half-waists (ω) using the relation (Saleh & Teich, 1991)

$$\omega^{\rm meas}(z) = {\rm FWHM}/(2\ln 2)^{1/2}. \quad (1)$$

Fig. 2(b) shows $\omega^{\rm meas}(z)$ as a function of z for the x (filled circles) and y (filled triangle) axes. The $\omega_x^{\rm meas}(z)$ and $\omega_y^{\rm meas}(z)$ distributions in Fig. 2(b) were fitted using a least-squares minimization to the function,

$$\omega^{\rm fit}(z) = \left\{[\omega(z)]^2 + \left(\omega_0^{\rm blur}\right)^2\right\}^{1/2}, \quad (2)$$

where $\omega(z)$ is the diffraction-limited value calculated from equation (5) and $\omega_0^{\rm blur}$ is an additional factor that accounts for the blurring factors such as mirror aberrations and also the point spread function (PSF) of the scintillation detector. The magnitude of $\omega_0^{\rm blur}$ was a free parameter in the fit and was found to be 2.1 ± 0.2 µm and 1.7 ± 0.2 µm in the x and y directions, respectively. The wavelength of the incident radiation was calculated from the incident X-ray energy, *e.g.* 18.5 keV yields $\lambda = 6.7 \times 10^{-8}$ mm.

As the presence of the PSF of the scintillation detector is a result of the measurement process, it must be deconvolved from $\omega_0^{\rm blur}$. The magnitude of the PSF was determined indirectly by scanning an Xradia X50-30-1CR test pattern with a beam energy E_0 = 18.5 keV. An image of the nickel (Ni) content of the 50 nm-diameter wires that form a grid pattern was isolated and fitted. Figs 3(a) and 3(b) show the horizontal (x) and vertical (y) profiles of a sub-section of the grid pattern, respectively. The calculated half-waists of the beam profile in the x and y directions were 1.6 ± 0.2 µm and 1.0 ± 0.2 µm,

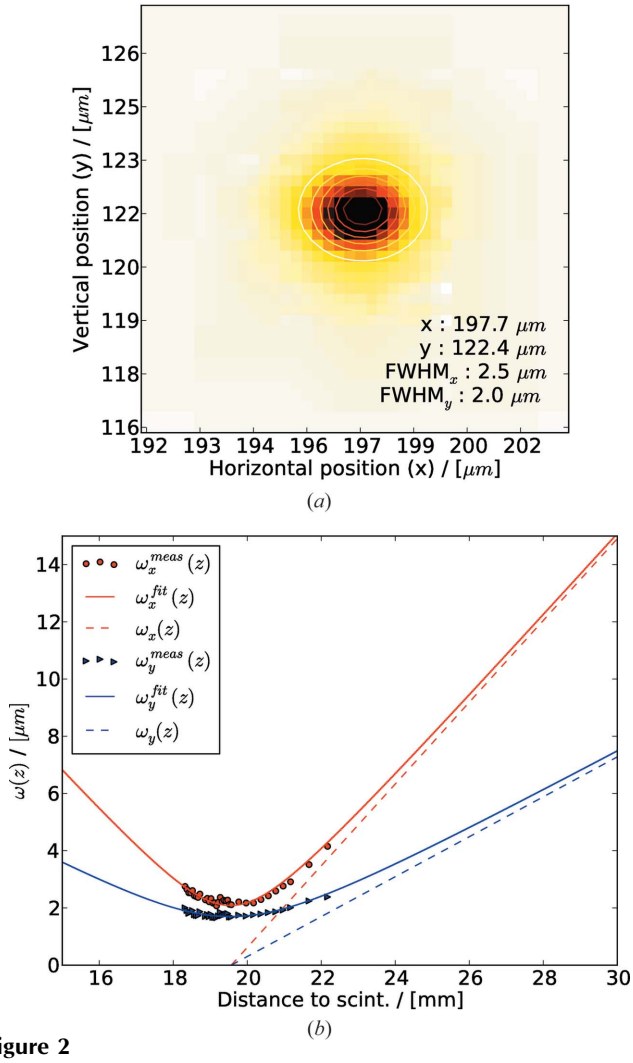

Figure 2
(a) XFM beam intensity profile at the focal plane, z = 51.6 mm. Overlaid on the distribution is an elliptical Gaussian fit. (b) A plot of Gaussian widths, $\omega(z)$, from profile fits as a function of scintillation detector offset along the z-axis. The filled circles and triangles are the experimentally measured widths for the horizontal and vertical beam components, respectively. The dashed lines are the diffraction-limited distributions [equation (5)]. The solid lines show the fits after the blurring term, $\omega^{\rm blur}(z)$, is included.

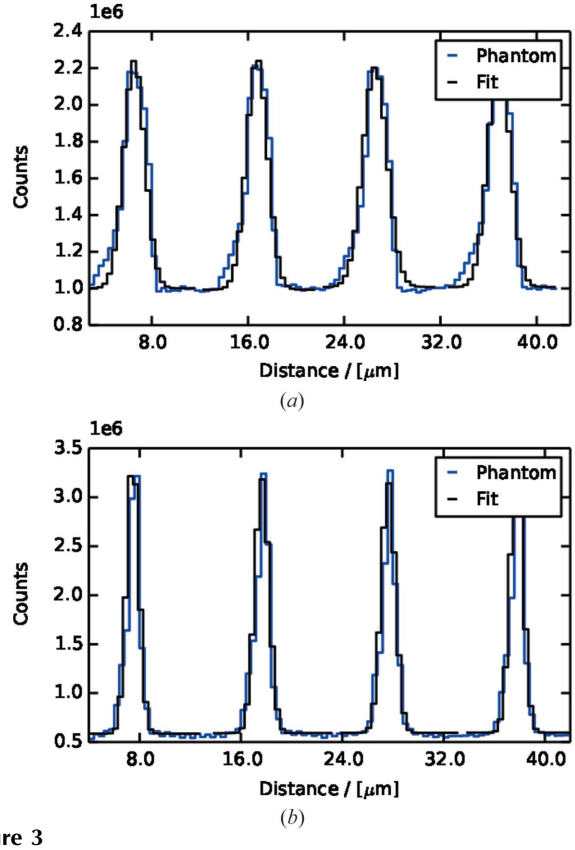

Figure 3
(a) and (b) show the x and y profiles of a sub-section of an image acquired by scanning an Xradia X50-30-1CR test pattern. The profiles are taken from the scan image of the Ni fluorescence content of the phantom collected with E_0 = 18.5 keV. Gaussian fits (black) are overlaid on the experimental data (blue).

respectively. Therefore, the PSF of the scintillation detector was calculated to be 0.8 ± 0.3 μm.

2.2. Experimental validation data

Experimental data were collected for three different incident X-ray beam energies: 18.5, 11.0 and 6.8 keV. For each scan, no calibration foil or sample was positioned in the sample mount, so the X-ray beam was propagating into free space. These data therefore primarily account for the detection of back-scatter from the air and fluorescence from interactions in the Maia detector housing.

The Maia detector data were analysed utilizing *GeoPIXE* (Ryan *et al.*, 1990; Ryan & Jamieson, 1993). The *GeoPIXE* software enables the user to process Maia X-ray event data, perform a pile-up correction, model X-ray yields from the sample and project deconvolved element concentration images using the dynamic analysis method (Ryan, 2000; Ryan *et al.*, 2010*b*). The result combines the events from all detector pixels to produce two-dimensional concentration images. An alternative feature utilized in this work is the ability to save the calibrated spectral data contained in each pixel as a 4096 channel histogram. These pixel-by-pixel histograms are then compared with the simulated data.

3. Monte Carlo model

In order to test the Monte Carlo simulation of the XFM end-station, X-rays were propagated from the exit of the focusing optics [**B** in Fig. 1(*b*)], through the detector and sample volumes and into free space. The model includes the Maia detector, optical table and nanoprobe and sample support structures. The nanoprobe support plate is mounted 1.5 m downstream of the Maia detector.

The simulation of the XFM end-station is comprised of a *Geant4* front-end and a Python back-end. Due to the low cross-sections and efficiency of the detectors, significant computation is required. The jobs are batch run on the Multimodal Australian ScienceS Imaging and Visualization Environment (MASSIVE) (Goscinski & Gureyev, 2011) computer cluster. The Python code accumulates the run data, combines the interactions and accounts for the experimental factors including blurring (through Gaussian convolution) due to the finite energy resolution of the Maia detector.

In *Geant4*, the incident particle is termed a `primary` (Geant4 Collaboration, 2012). The energy, momentum, polarization and origin are all specified by setting the appropriate attributes. The `primaries` for this XFM model are an incident beam of linearly polarized low-energy X-rays in the range $4 \leq E_0 \leq 20$ keV. For a randomly polarized source, the highest-accuracy low-energy electromagnetic physics package is the `G4EmStandardPhysics_option4` class (Ivanchenko *et al.*, 2014). However, this class does not incorporate polarization effects of the incident photons and so the `G4EmLivermorePolarizedPhysics` class was instantiated instead. The step thresholds for the electron and photon propagation were reduced to 0.1 μm in order to reproduce the correct low-energy spectral distribution. Setting the threshold to this level ensures that a particle with the corresponding threshold energy is absorbed after travelling this distance, therefore limiting the production of secondary particles to an acceptable level.

The *Geant4* simulation initializes each photon at a location $\mathbf{r}_{i,j,k}$ with a momentum directional unit vector of $\mathbf{p} = (0,0,1)$ and a polarization vector of $\boldsymbol{\varepsilon} = (1,0,0)$. Simulations were performed with both the Gaussian beam class and also an incident 1.5 μm-diameter pencil beam. Both instances of the simulation showed similar results. However, as the Gaussian beam formalism is physically motivated and more general in application, the results presented herein were derived using the class detailed in Appendix *A*2.

The Gaussian beam class modifies $\mathbf{p}$ to a paraxial value $\mathbf{p}'$; therefore, $\boldsymbol{\varepsilon}$ must also be modified accordingly. The polarization direction is calculated on a per-event basis using the Rodrigues rotation formula (Goldstein, 1980), such that

$$\boldsymbol{\varepsilon}' = \boldsymbol{\varepsilon}\cos\theta + (\boldsymbol{\omega} \wedge \boldsymbol{\varepsilon})\sin\theta + \boldsymbol{\omega}(\boldsymbol{\omega} \cdot \boldsymbol{\varepsilon})(1 - \cos\theta), \quad (3)$$

where $\boldsymbol{\omega}$ is the unit vector describing the axis of the rotation calculated from the cross product $\boldsymbol{\omega} = \mathbf{p} \wedge \mathbf{p}'$, $\cos\theta = \mathbf{p} \cdot \mathbf{p}'$, and the cross product in the second term in (3) is not normalized.

The position vector is also blurred (convolved with a Gaussian) to account for experimental factors such as mirror aberrations. The x and y emission locations are re-sampled from independent normal distributions with standard deviations $\omega_{0,x}^{\rm blur}$ and $\omega_{0,y}^{\rm blur}$, respectively. The blurring parameters, calculated from the measurements described in §2.1, were found to have the values $\omega_{0,x}^{\rm blur} = 1.3$ μm and $\omega_{0,y}^{\rm blur} = 0.9$ μm.

The experimental hall that contains the physical beamline infrastructure is defined in a `DetectorConstruction` class. The materials, sizes and locations of all components must be precisely defined. The composition of the air in the experimental hall was found to have a measurable effect. The levels of argon (Ar), xenon (Xe) and krypton (Kr) were taken to be 0.93%, 8.7×10^{-6}% and 1.0×10^{-4}%, respectively (Hein & Arena, 2010). The fraction-by-mass elemental concentrations were calculated from these values for use in the simulation. The Be used for the entrance and exit windows was type IF-1 supplied by Materion. The stainless steel was of the standardized type 316 (316-SS). The fraction-by-mass elemental concentrations of the Be and 316-SS were calculated from the maximum percentage values in the ranges specified by the manufacturers.

3.1. Simulation data

In order that a comparison with the experimental data could be made, the simulated spectra from each of the 384 pixels were individually corrected (blurred) by an energy-dependent function. The blurring function for each channel was measured during the detector configuration process from fits applied by the *GeoPIXE* software. Fig. 4(*a*) shows the blurring function for detector pixel number 78 [#78, see Fig. 9(*a*)]. The resolution of the Maia 384A detector (detailed in this work) has been greatly improved lately, and the XFM

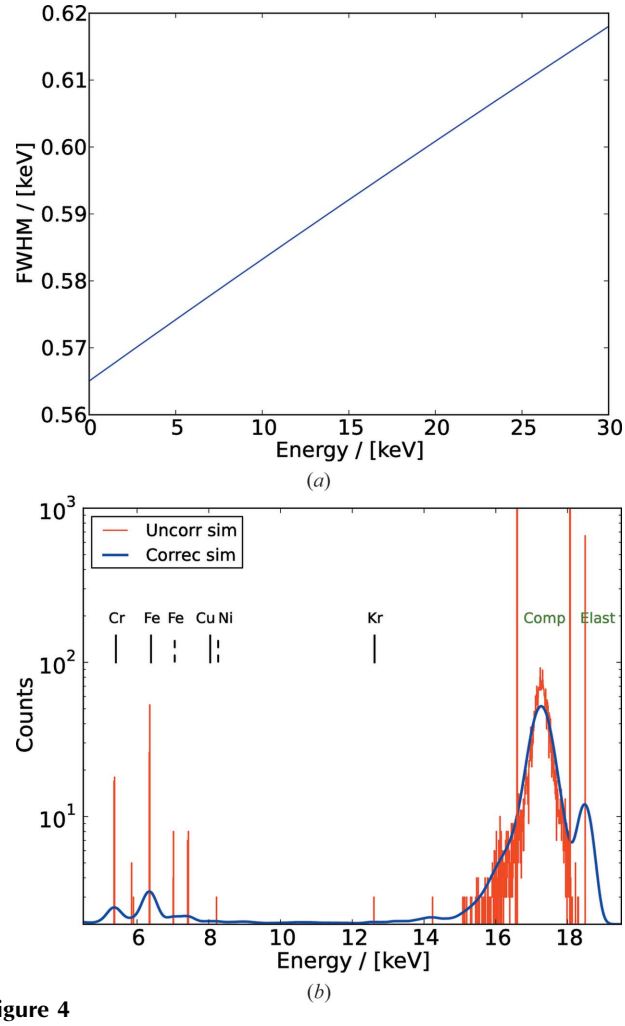

Figure 4
(*a*) Blurring function for detector pixel 78 as a function of spectrum energy. (*b*) The simulated energy spectrum for pixel 78 from the propagation of 18.5 keV X-rays through the XFM end-station. No sample was present. Both the uncorrected (red) and corrected (blue) spectra are displayed. The $K\alpha$ and $K\beta$ lines of the fluorescence emission from X-ray interactions in the detector housing and air are shown with solid and dashed lines, respectively. The regions of the spectra that correspond to Compton and elastic back-scatter are also indicated.

unit will be replaced shortly with the improved 384B (Dyl *et al.*, 2014; Ryan *et al.*, 2014).

Spectra were produced from simulations of the propagation of 18.5 keV X-rays through the XFM end-station with no sample mounted in the sample stage. Fig. 4(*b*) presents the simulated spectrum for #78 before (red) and after (blue) application of the blurring function. Fluorescence emissions resulting from the interaction of X-rays in the detector housing and air are also shown. The Compton and elastic back-scatter regions of interest (ROIs) are indicated.

4. Discussion

Assessment of the performance of the Monte Carlo model has been performed through the comparison of simulated and experimental spectral distributions. Fig. 5 shows the experimental and simulated total integrated spectra for all Maia

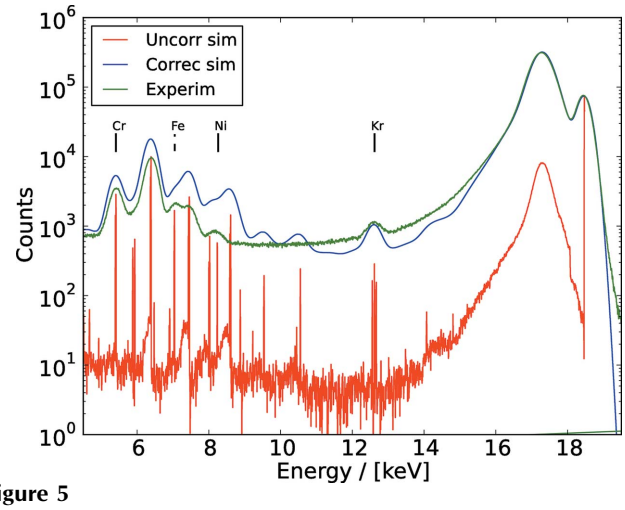

Figure 5
Comparison of the experimental and simulated total integrated spectra for all Maia detector pixels for E_0 = 18.5 keV. No sample was mounted. The elemental concentrations of the impurities in both the Be-window and stainless steel housing of the Maia detector were set to the maximum range-bound values.

detector pixels for E_0 = 18.5 keV, with no sample mounted in the beam path. The simulated and experimental distributions show qualitatively good agreement in the Compton and elastic scatter regions. However, agreement in the fluorescence region, where incident X-rays are back-scattered into the detector housing and subsequently interact yielding the emission of fluorescence X-rays, is poor.

The three components specified in the `DetectorConstruction` file that primarily influence the fluorescence distributions are the air, Be-window and 316-SS detector housing. The contribution to spectral intensity from Cr, Mn, Fe, Ni, Zn and Pb are significantly overestimated in the simulation. The levels of the impurities in 316-SS are specified within a tight range and the detector is well shielded due to the use of aluminium nitride (AlN) structures, also included in the model. The detector response is, however, sensitive to the concentrations of the impurities in the Be window. To obtain the best match across the three incident energies, the fraction-by-mass concentrations were adjusted down from the maximum range-bound values to improve the match [see Fig. 6(*a*)]:

$$\begin{aligned}
\text{Cr}&: 0.020\% \rightarrow 0.008\%,\\
\text{Fe}&: 0.185\% \rightarrow 0.052\%,\\
\text{Ni}&: 0.129\% \rightarrow 0.018\%,\\
\text{Zn}&: 0.072\% \rightarrow 0.003\%,\\
\text{Mn}&: 0.018\% \rightarrow 0.003\%,\\
\text{Pb}&: 0.011\% \rightarrow 0.001\%.
\end{aligned}$$

Figs. 6(*b*) and 6(*c*) show the per pixel intensity in the fluorescence ROI $4.5 \leq E_{\rm ROI} \leq 9.0$ keV for the experimental and simulated data that constitute Fig. 6(*a*). The intensity distributions show very close agreement and both include the asymmetry in the intensity in the vertical direction due to the

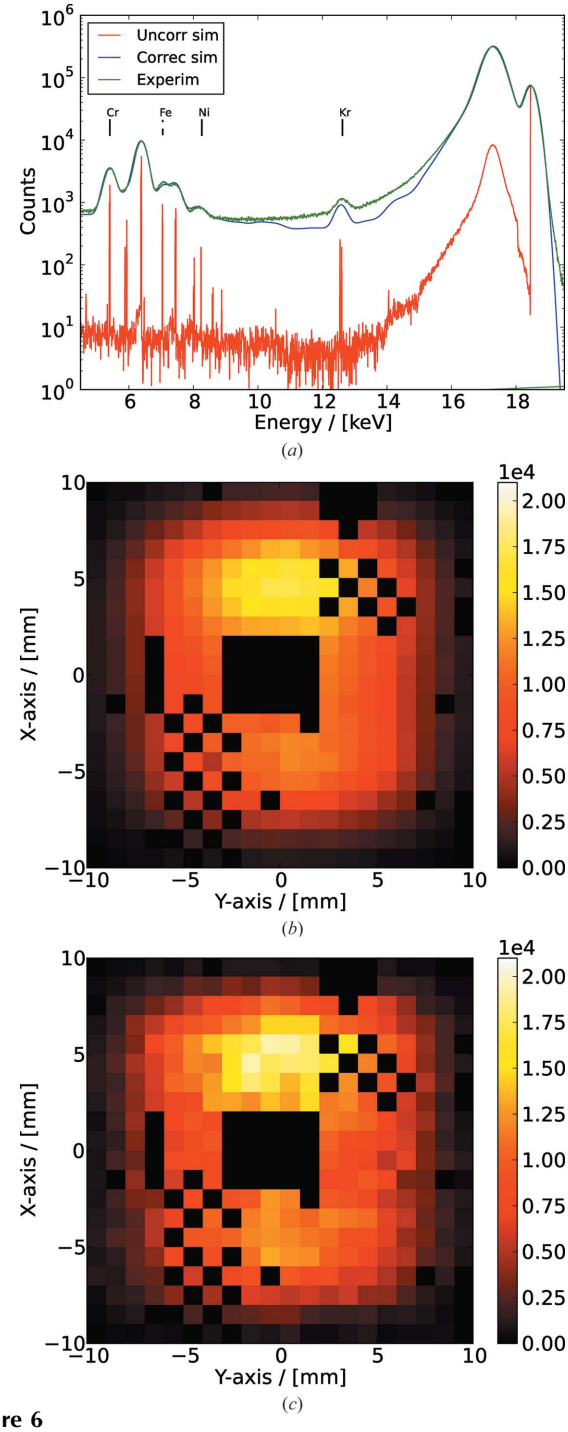

Figure 6
(*a*) Comparison of the experimental and simulated total integrated spectra for all Maia detector pixels for E_0 = 18.5 keV. No sample was mounted. The elemental concentrations of Cr, Mn, Fe, Ni and Zn were reduced with respect to those for the simulation in Fig. 5. Images of the per pixel intensity in the fluorescence ROI 4.5 $\leq E_{\rm ROI} \leq$ 9.0 keV for the experimental (*b*) and simulated (*c*) data.

elevation angle of the beam as it propagates away from the KB mirror pair.

Following the adjustments described above, the fluorescence ($E_{\rm ROI} \leq 9.0$ keV) and scatter regions show good agreement. There is, however, still a discrepancy in the ROI 9.0 < $E_{\rm ROI} \leq$ 16.8 keV, where 16.8 keV corresponds to the minimum single Compton back-scatter energy for the calculated acceptance angle of the Maia detector. The simulation significantly underestimates the intensity in this region, excluding the Kr fluorescence peak. This discrepancy is found to be isotropic in its position dependence across the detector and corresponds to the range in which the *L*-edges of materials on the PCBs and in electrical connections would be found, *e.g.* gold (Au).

Fig. 7 shows the experimental and simulated total integrated spectra for all Maia detector pixels for E_0 = 11.0 and 6.8 keV. Similar trends are observed to those previously discussed for Fig. 6(*a*). Again, the discrepancies are small compared with the qualitative match in the scatter regions and are the result of the fundamental limitations in the accuracy of the model. These discrepancies are isotropic in their position dependence and will be dwarfed by orders of magnitude by the fluorescence intensities detected when a foil is actually positioned in the sample stage.

As the ability of the simulation to faithfully reproduce the shape and magnitude of the scatter distributions is the most challenging aspect of modelling an experimental configuration such as that detailed in this work, the remainder of the discussion focuses on this aspect of the work.

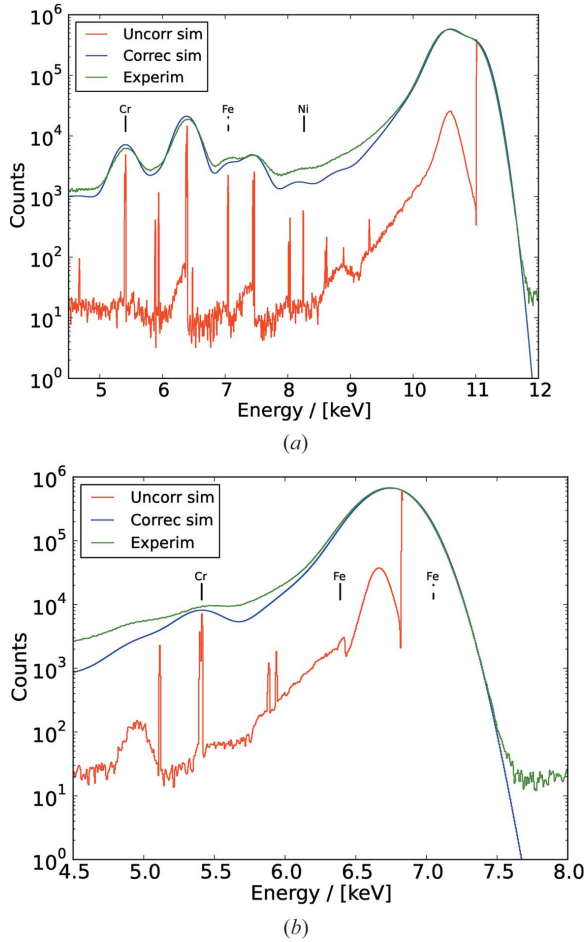

Figure 7
Comparison of the experimental and simulated total integrated spectra for all Maia detector pixels for E_0 = 11.0 (*a*) and 6.8 keV (*b*).

Fig. 8(*a*) shows the number of counts in the Compton ROI on a per pixel basis, as a function of Cartesian pixel position. The central hole (described in §2) and also the pixels omitted in this work (31 of the 384) are coloured black. Some omitted pixels are faulty while others have losses (up to 30%) caused by photon readout artefacts in the Revision A Maia detector, which are beyond the scope of the modelling here.

The white dashed lines show a fourfold symmetry in the distribution. The increased intensity along the line $y = 0.0$ mm is primarily due to the horizontal beam divergence. The intensity along the line $x = 0.0$ mm is due to both the (lesser) divergence and increased scattering cross-section in the vertical direction for horizontally polarized photons. Fig. 8(*b*) shows the number of counts in the Compton ROI as a function of angular pixel location for the experimental (black) and simulated (red) data. Qualitatively, the distributions show good agreement, especially for peripheral pixels where the intensities are lower. This also corresponds to regions where the scattering angle is greater, for a constant distance, z, from the detector.

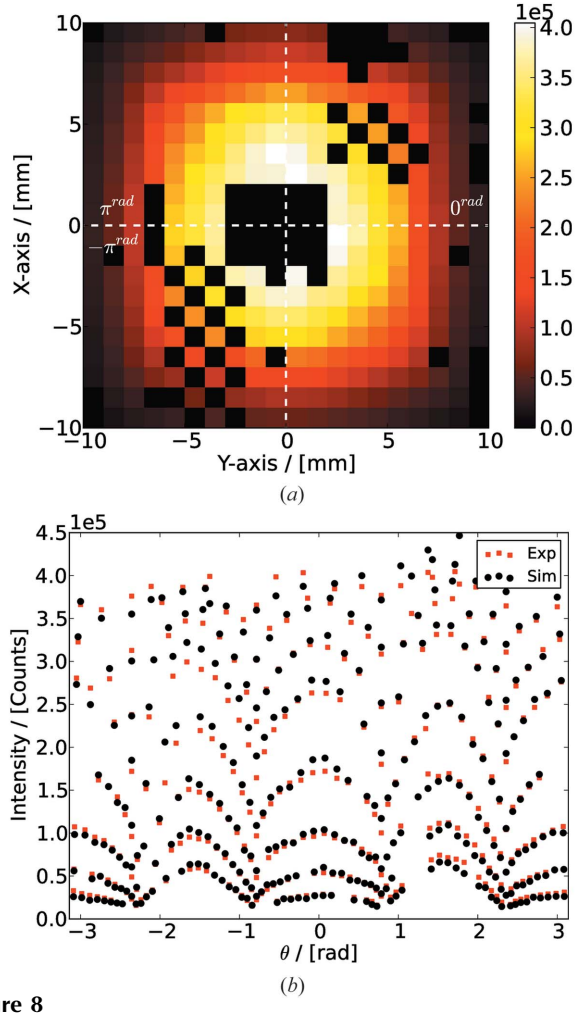

Figure 8
Number of counts (intensity) in the Compton ROI on a per pixel basis. (*a*) The measured intensities, presented as a function of Cartesian pixel position. The central gap and faulty pixels are displayed in black. (*b*) Intensities from experiment (black) and simulation (red) as a function of angular pixel location.

Fig. 9 shows some example comparisons of experimental (green) and simulated (blue) spectral distributions that include the Compton and elastic back-scatter peaks. The comparisons are presented for four pairs of pixels that are equidistant from the $y = x$ line of symmetry through the detector.

The metric chosen for quantification of the relative agreement between the two data sets is the reduced χ-squared (Hurtado *et al.*, 2004),

$$\chi^2_{\rm red} = \frac{1}{n-p-1}\sum_{i=0}^{n}\left\{\frac{\left[S_1(i)-S_2(i)\right]^2}{\sigma(i)^2}\right\} \qquad (4)$$

where $S_1(i)$ and $S_2(i)$ are the experimental and simulated spectra, respectively, n is the number of spectral bins in the ROI, p is the number of free parameters and $\sigma(i) = [S_1(i)]^{1/2}$ is the uncertainty associated with spectral bin i.

Values for the $\chi^2_{\rm red}$ parameterization should ideally equal unity. The values calculated for the distributions in Fig. 9 are displayed above each respective peak. The $\chi^2_{\rm red}$ magnitudes show better agreement for the elastic peaks than for the Compton peaks. This is attributed to the fact that the elastic peaks were used as a point of reference in the initial gain calibration as they remain fixed. Conversely, the peak value and shape of each Compton distribution depends on both the incident energy and geometry of the experimental configuration. Visually, the experimental and simulated Compton distributions are seen to agree well. However, the $\chi^2_{\rm red}$ parameter is sensitive to small misalignments (energy shifts) between the distributions. These misalignments are attributed to uncertainties in the gain matching process.

In order to obtain a more holistic measure of the accuracy with which the simulation reproduces the experimental data, the $\chi^2_{\rm red}$ values were histogrammed. Fig. 10(*a*) supports the previous observation that the $\chi^2_{\rm red}$ magnitudes show better agreement for the elastic peaks than for the Compton peaks. The histogram of data for the elastic peaks shows tighter grouping and is peaked at unity.

The data collected for an incident X-ray energy of 18.5 keV have been compared with equivalent datasets collected at 11.0 and 6.8 keV beam energies. As the beam energy is reduced, so too is the separation between the elastic and Compton back-scatter peaks. At 11.0 keV, the scatter peaks (using the Maia 384A detector) are inseparable without the aid of a sophisticated fitting routine. Therefore, the $\chi^2_{\rm red}$ metric has been calculated for a combined Compton plus elastic scatter ROI. These values were calculated for each of the incident beam energies and histogrammed. Fig. 10(*b*) shows the resulting histograms. From Fig. 10(*b*) it can be seen that $\chi^2_{\rm red}$ becomes more spread as the incident beam-energy decreases. This spreading is attributed to two factors: (i) the fact that the width of the combined Compton-elastic ROI decreases as the incident energy decreases and so the $\chi^2_{\rm red}$ metric is more sensitive to noise and misalignment; (ii) the observation that the low energy-tailing in the Compton back-scatter distribution is less faithfully reproduced at lower incident energies.

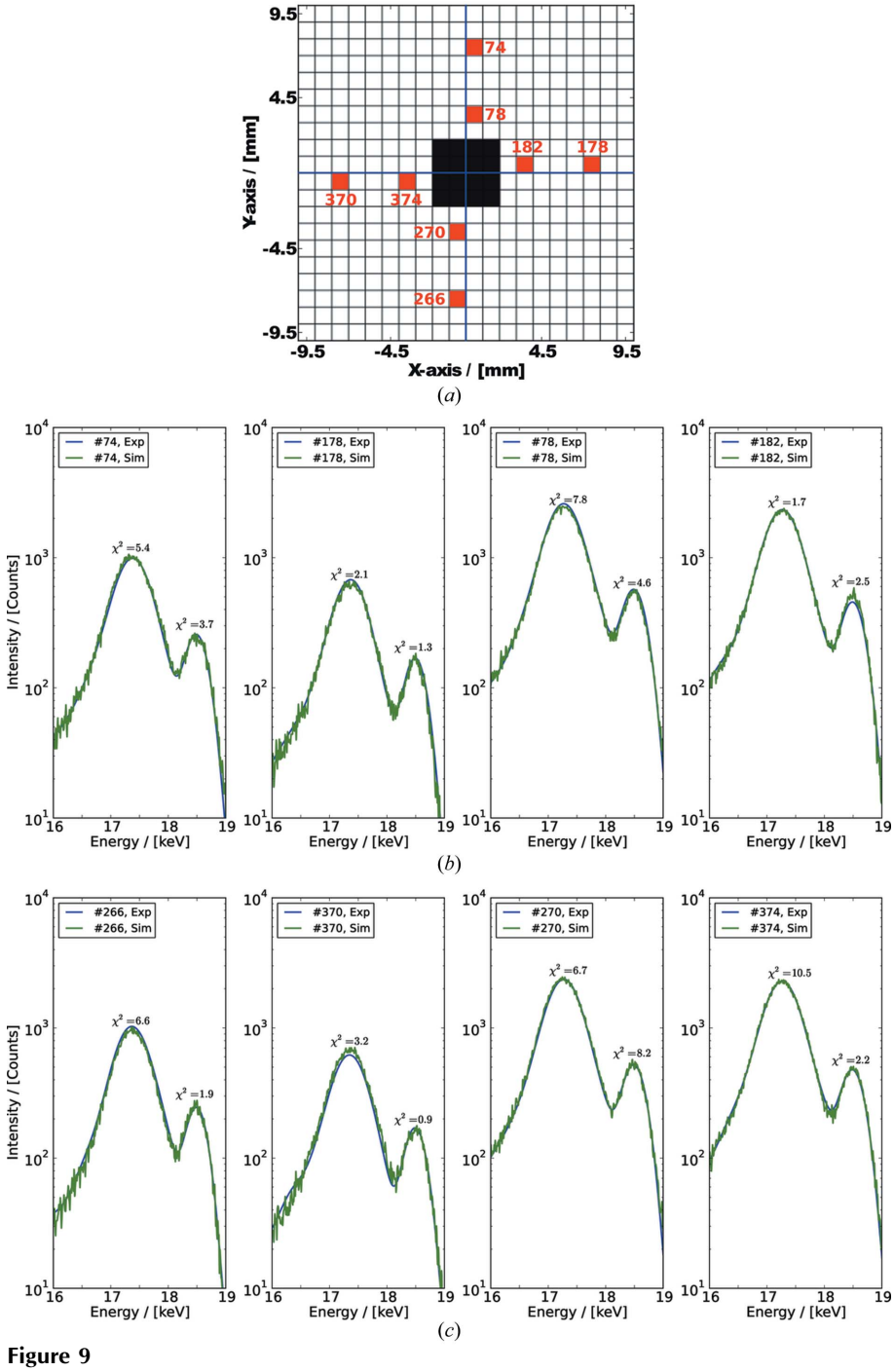

Figure 9
Comparisons of experimental (green) and simulated (blue) spectral distributions, for four pairs of detector pixels positioned either side of the $y = x$ line of symmetry. The $\chi^2_{\rm red}$ metric is displayed for both the Compton and elastic back-scatter peaks. (*a*) Diagram of selected pixel locations. (*b*) Spectra for pixel numbers #74, #178, #78 and #182, in the upper right quadrant. (*c*) Spectra for pixels #266, #370, #270 and #374, in the lower left quadrant.

Figs. 11(*a*) and 11(*b*) show comparisons between the experimental and simulated spectra for the upper-right quadrant of the Maia detector [analogous to those presented in Fig. 9(*b*)] for incident X-ray energies of 11.0 and 6.8 keV, respectively. It can be seen that, as the incident X-ray energy decreases, the agreement between the experimental and simulated data for the low-energy Compton tail diverges. This is attributed to computational difficulties in the Monte Carlo software with respect to reproducing the effects of multiple scattering. It is known (Pratt *et al.*, 2007, 2010) that there are significant limitations in the photon scattering models when the momentum transfer of the X-ray approaches the target atomic shell binding energy. The cut values in *Geant4*, for both photons and electrons, were reduced to 0.001 µm in order to eliminate these parameters as a possible source of error.

5. Conclusion

A *Geant4* simulation of the XFM end-station at the Australian Synchrotron was developed and compared with experimental data collected at three incident beam energies: 18.5, 11.0 and 6.8 keV. The simulation incorporates a newly developed general Gaussian beam class that accounts for the physically measured beam profile that propagates from the exit of the KB mirror pair. Parameters for initializing the beam were extracted from fits to experimental data, as discussed in §2.1.

The simulation is shown to reproduce the shape of the fluorescence spectral distributions that result from interactions of incident and back-scattered X-rays in the air, Maia detector housing, optical table and nanoprobe and sample support structures. The main limitations of the model are in reproducing the transition of the Compton back-scatter low-energy tail into the fluorescence background and also in accounting for some of the fluorescence emissions in the range $9.0 < E_{\rm ROI} \leq 16.8$ keV.

The limitations of the low-energy photon scattering models, under these conditions, are known to the *Geant4* low-energy electromagnetic physics working group. An extended version of the Monash Compton scattering model that addresses the observed issues is currently under development (Brown *et al.*, 2014).

The limitations in reproducing some of the *L*-edge emissions from materials (*e.g.* Au) found on PCBs and electrical connections are difficult to explicitly account for. The experimental end-station contains many components that may contribute to the general background and one possible solution is to fit a correction factor to the pixel-by-pixel spectra as

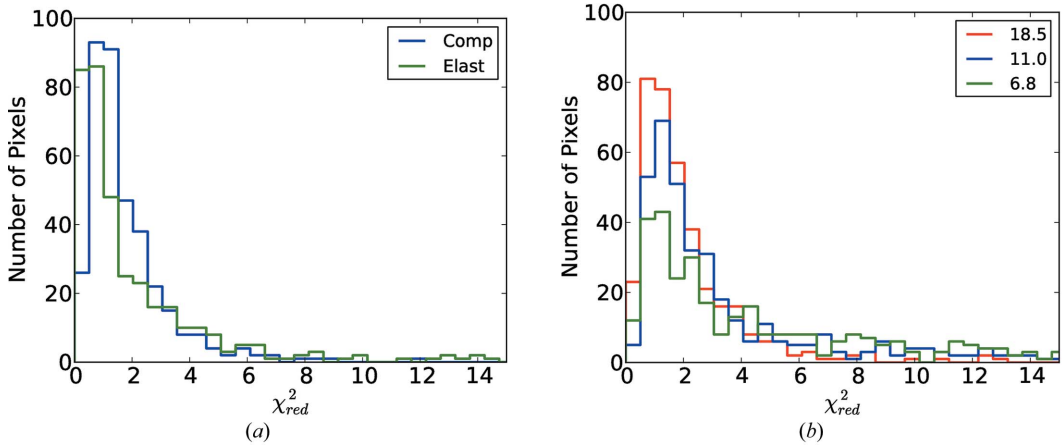

Figure 10
Reduced-χ^2 comparisons of the experimental to simulated spectra for three incident X-ray beam energies: 18.5, 11.0 and 6.8 keV.

the contributions are found to vary isotropically across the Maia detector. It should also be noted that these discrepancies will be dwarfed by the fluorescence contributions that occur when a sample is actually positioned in the sample stage.

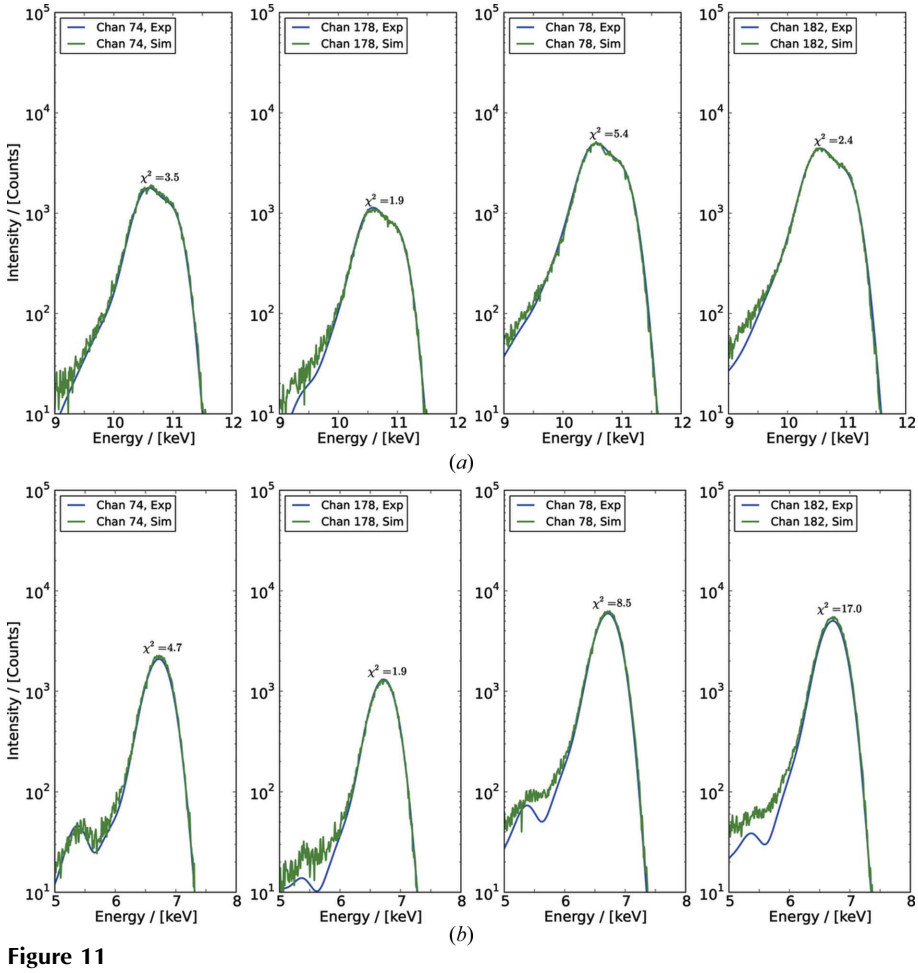

Figure 11
Comparisons of experimental (green) and simulated (blue) spectral distributions, for four pairs of detector pixels positioned either side of the $y = x$ line of symmetry. The χ^2_{red} metric is displayed for the ROI that spans the summation of the Compton and elastic back-scatter ROIs. The spectra for pixel numbers #74, #178, #78 and #182, in the upper-right quadrant, are shown for incident beam energies of (*a*) 11.0 and (*b*) 6.8 keV.

APPENDIX *A*

The propagation algorithm presented in this section builds on the work performed by Canestrari *et al.* (2014) and develops a novel means for calculating the phase gradient used to initialize the emission direction of the rays in the simulation. The calculation is incorporated into a simple C++ class for use in Monte Carlo simulations of focused monochromatic X-ray beams in order that parameters such as the beam waist and focal depth are accounted for.

A Gaussian beam (Chalupský *et al.*, 2010) is typically described in terms of its half-waist as a function of propagation distance along the z-axis. The half-waist, $\omega(z)$, is defined as the radius at which the beam amplitude and intensity falls to $1/e$ and $1/e^2$ of their peak values (Saleh & Teich, 1991), respectively. The magnitude of the half-waist is given by

$$\omega(z) = \omega_0\left[1 + \left(\frac{z - z_0}{z_R}\right)^2\right]^{1/2}, \quad (5)$$

where

$$z_R = \pi\omega_0^2/\lambda \quad (6)$$

is the Rayleigh range parameter and ω_0 is the minimum half-waist (at $z = z_0$); this corresponds to the radial waist for a cylindrically symmetric Gaussian beam.

A1. Hermite–Gaussian beam model

The propagation of paraxial (Lax *et al.*, 1975) monochromatic beams with elliptical intensity cross-sections can be described by the Hermite formalism. The equation for the spatial part of the complex scalar (electric) field of a

Hermite–Gaussian beam is given by (Siegman, 1986)

$$\psi(x,z)=\left[\frac{2}{\pi\omega_x^2(z)}\right]^{1/4}\exp\left[-\frac{x^2}{\omega_x^2(z)}\right]\exp\left[-\frac{i\pi x^2}{\lambda R_x(z)}+\frac{i\varphi_{0x}(z)}{2}\right] \tag{7}$$

where

$$R_x(z)=z+\frac{1}{z}\left(\frac{\pi\omega_{0x}^2}{\lambda}\right)^2, \tag{8}$$

$$\varphi_{0x}(z)=\tan^{-1}\left(\frac{\lambda z}{\pi\omega_{0x}^2}\right), \tag{9}$$

$\omega_x(z)$ is the half-waist parameterization confined to the x–z plane and ω_{0x} is the minimum of the half-waist in the x–z plane.

The profiles $\psi(x,z)$ and $\psi(y,z)$ are the cross sections over two orthogonal planes, where $\psi(y,z)$ is also obtained from equation (7) with the appropriate interchange of notation ($x \rightarrow y$). The two-dimensional beam profile is then calculated as

$$\psi(\mathbf{r})=\psi(x,y,z)=\psi(x,z)\,\psi(y,z)\exp(ikz), \tag{10}$$

where

$$r=\left(x^2+y^2+z^2\right)^{1/2}\approx z+\frac{x^2+y^2}{2z}, \tag{11}$$

accounts for the paraxial approximation. Equation (10) gives a complex expression from which the magnitude [$R = |\psi(\mathbf{r})|$] and phase {$\varphi = \arg[\psi(\mathbf{r})]$} of the X-rays at each emission location can be extracted. R and $\nabla\varphi(\mathbf{r})$ will ultimately be utilized to determine the emission location and direction of the propagating X-rays, as R is proportional to the probability of emission and $\nabla\varphi(\mathbf{r})$ is the direction of emission.

Fig. 12(*a*) shows the phase distribution calculated on the emission plane arbitrarily chosen to be 3.0 mm upstream of the focal plane, *i.e.* $z = z_0 - Z$ where Z = 3.0 mm. The X-ray beam energy was selected to be 18.5 keV. In Fig. 12(*b*) the dot-dashed line shows the slice profile through this data along the line y = 0.0 mm. The phase is shown within the principal branch (Fried & Vaughn, 1992) with the branch cut at $-\pi$ and π. As the components of the emission direction will be calculated from the three-dimensional gradient of the phase [$\nabla\varphi(\mathbf{r})$], determined through numerical differentiation, the phase distribution wrapped to the interval $-\pi \leq \varphi(\mathbf{r}) < \pi$ is not ideal. There exist techniques for unwrapping phase branches (Ghiglia & Romero, 1994); however, these require additional computational steps. An alternate means for calculating the ray-direction is derived in the following section.

A1.1. Wave mechanics derivation. Consider the complex field

$$\Psi(\mathbf{r},t)=A(\mathbf{r},t)\exp[i\Phi(\mathbf{r},t)], \tag{12}$$

where $A(\mathbf{r},t)$ is the amplitude, $\Phi(\mathbf{r},t)$ is the phase and t is the time. Using the chain rule, the gradient of (12) is

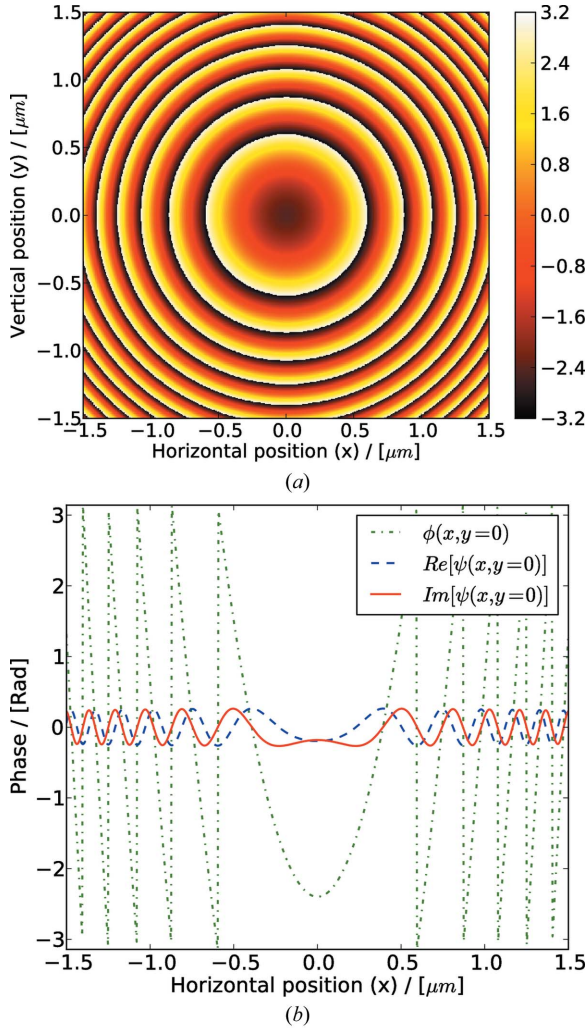

Figure 12
(*a*) Phase distribution {$\varphi = \arg[\psi(\mathbf{r})]$} calculated from equation (10) on the plane $z = z_0 - 3.0$ mm. (*b*) Slice data. The dashed line shows the slice through the data in (*a*) along y = 0.0 mm. Overlaid are the slices through the real and imaginary components of the two-dimensional distributions calculated from equation (16).

$$\nabla\Psi(\mathbf{r},t)=iA(\mathbf{r},t)\exp[i\Phi(\mathbf{r},t)]\nabla\Phi(\mathbf{r},t)+\exp[i\Phi(\mathbf{r},t)]\nabla A(\mathbf{r},t). \tag{13}$$

Multiplying (13) through by the complex conjugate of (12), taking only the imaginary part, and subsequently rearranging for $\nabla\Phi(\mathbf{r},t)$ yields

$$\nabla\Phi(\mathbf{r},t)=\frac{\mathrm{Im}[\Psi^*(\mathbf{r},t)\,\nabla\Psi(\mathbf{r},t)]}{A^2(\mathbf{r},t)}. \tag{14}$$

Finally, substituting (10) into (14) and adjusting the notation such that

$$\begin{aligned}\Psi(\mathbf{r},t) &\rightarrow \psi(x,y,z)\exp(-i\omega t)\\ &= A(x,y,z)\exp[i\varphi(x,y,z)]\exp(-i\omega t),\end{aligned} \tag{15}$$

where ω is the angular frequency, gives

$$\nabla\varphi(x, y, z) = \mathrm{Im}[\psi^*(x, y, z)\nabla\psi(x, y, z)] \Big/ \left\{\left[\frac{2}{\pi\omega_x^2(z)\omega_y^2(z)}\right]^{1/2} \exp\left(-\frac{x^2}{\omega_x^2} - \frac{y^2}{\omega_y^2}\right)\right\}^2 = \mathbf{p}_{i,j,k}. \quad (16)$$

Here, $\mathbf{p}_{i,j,k}$ is used to represent the momentum directional unit vector in the three Cartesian directions, i, j and k. Equation (16) shows that the gradient of the phase can be obtained from the gradient of the complex function $\psi(x, y, z)$, as opposed to the direct numerical differentiation of $\varphi(x, y, z)$ presented in Appendix *A*1. The advantage of this method is apparent when the variation in both the real and imaginary components of ψ are overlaid on the profile for $\varphi(x, y = 0)$ from Fig. 12(*a*). The dashed and solid lines in Fig. 12(*b*) show $\mathrm{Re}[\psi(x, y = 0)]$ and $\mathrm{Im}[\psi(x, y = 0)]$, respectively. It is immediately clear that numerical differentiation of these smoothly varying curves is much less prone to errors; there is no longer the abrupt change resulting from the $-\pi \leq \varphi(\mathbf{r}) < \pi$ wrapped phase distribution in Fig. 12(*a*).

It should be noted that this formalism holds for the case of a simple Gaussian analytical model approximating the input radiation. In the case of numerical wavefront propagation, resolving for the electric field would require the use of a very dense transverse mesh.

A2. Gaussian beam propagation

A C++ implementation of this beam propagation technique has been developed for incorporation into Monte Carlo simulations. The implementation [see Fig. 13(*a*)] utilizes the matrix manipulation functionality of Blitz++ (Veldhuizen, 1998) and the built-in grad3dn function for fast calculation of the components of equation (16). The algorithm computes the emission location ($\mathbf{r}_{i,j,k}$) and momentum directional unit vector ($\mathbf{p}_{i,j,k}$) components for the emission of X-rays, from an arbitrary z-plane, using a multi-step sequence of calculations [outlined in Fig. 13(*a*)]:

(i) Determine $\mathbf{r}_{i,j,k}$: sample the x and y emission locations, over a given plane of constant z, from independent normal distributions with standard deviations calculated from $\omega_x(x)$ and $\omega_y(x)$, respectively.

(ii) Calculate the Hermite–Gaussian beam values: use equation (10) to determine $\psi(x, y, z)$ on a $5 \times 5 \times 5$ matrix centred at $\mathbf{r}_{i,j,k}$.

(iii) Determine the components of the momentum (emission direction) $\mathbf{p}_{i,j,k}$: calculate the numerical three-dimensional gradient on the matrix and also calculate the remaining parameters in equation (16).

(iv) Blur $\mathbf{r}_{i,j,k}$ to account for experimental (blurring) factors by convolution with a Gaussian: re-sample the x and y emission locations from independent normal distributions with standard deviations calculated from $\omega_{0,x}^{\mathrm{blur}}$ and $\omega_{0,y}^{\mathrm{blur}}$, specified by the user. The addition of this blurring term makes this implementation equivalent to the Gaussian Schell model (Starikov & Wolf, 1982).

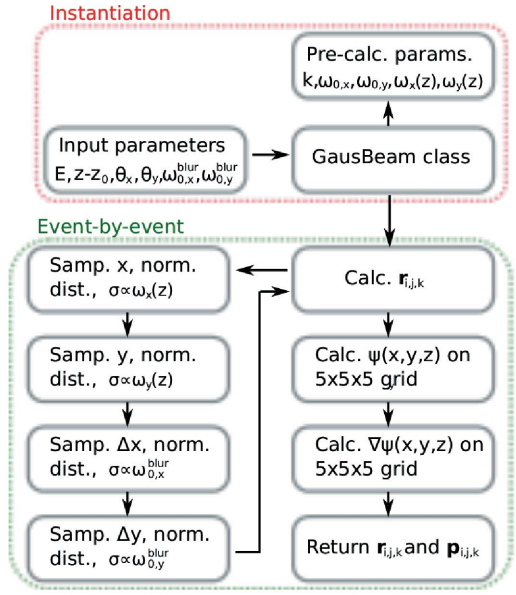

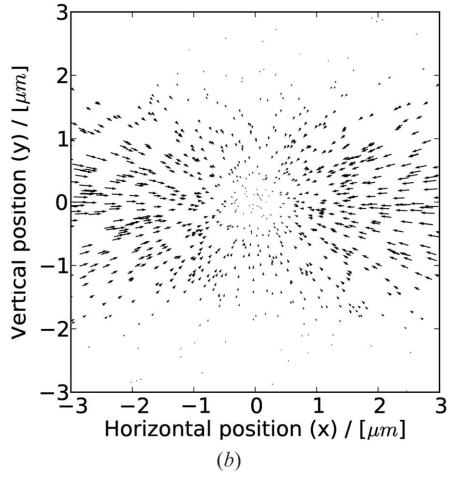

Figure 13
(*a*) Flow diagram showing calculation of the emission location ($\mathbf{r}_{i,j,k}$) and momentum directional unit vector ($\mathbf{p}_{i,j,k}$) components. (*b*) A quiver plot showing the x–y component of each vector, $\mathbf{p}_{i,j}$, for 1000 initialized 18.5 keV X-ray trajectories emitted from the plane $z = z_0 - 3.0$ mm. The minimum waists are $\omega_{0,x}$ = 0.015 µm and $\omega_{0,y}$ = 0.031 µm. No blurring factors have been included.

Fig. 13(*b*) shows the projection of the momentum directional unit vectors onto the x–y plane for 1000 randomly initialized 18.5 keV X-rays, calculated from the phase distribution presented in Fig. 12(*a*). The minimum waists are $\omega_{0,x}$ = 0.015 µm and $\omega_{0,y}$ = 0.031 µm. No blurring factors were included.

The authors would like to acknowledge the Australian Synchrotron XFM beamline staff for technical support, and the Australian Synchrotron for approving beam time. This work was also supported by the Multi-modal Australian ScienceS Imaging and Visualization Environment (MASSIVE) (see http://www.massive.org.au).

References

Agostinelli, S. *et al.* (2003). *Nucl. Instrum. Methods Phys. Res. A*, **506**, 250–303.

Allison, J. *et al.* (2006). *IEEE Trans. Nucl. Sci.* **53**, 270–278.

Brown, J., Dimmock, M., Gillam, J. & Paganin, D. (2014). *Nucl. Instrum. Methods Phys. Res. B*, **338**, 77–88.

Canestrari, N., Chubar, O. & Reininger, R. (2014). *J. Synchrotron Rad.* **21**, 1110–1121.

Chalupský, J. *et al.* (2010). *Opt. Express*, **18**, 27836–27845.

de Jonge, M. D. *et al.* (2010). *Proc. Natl Acad. Sci.* **107**, 15676–15680.

de Jonge, M. D. & Vogt, S. (2010). *Curr. Opin. Struct. Biol.* **20**, 606–614.

Donner, E., Punshon, T., Guerinot, M. L. & Lombi, E. (2012). *Anal. Bioanal. Chem.* **402**, 3287–3298.

Dyl, K. A., Cleverley, J. S., Bland, P. A., Ryan, C. G., Fisher, L. A. & Hough, R. M. (2014). *Geochim. Cosmochim. Acta*, **134**, 100–119.

Fried, D. L. & Vaughn, J. L. (1992). *Appl. Opt.*, **31**, 2865–2882.

Geant4 Collaboration (2012). *GEANT4*, http://geant4.web.cern.ch/geant4/.

Ghiglia, D. C. & Romero, L. A. (1994). *J. Opt. Soc. Am. A*, **11**, 107–117.

Goldstein, H. (1980). *Classical Mechanics*. Reading, MA: Addison-Wesley.

Goscinski, W. & Gureyev, T. (2011). *eResearch Australasia Conference.*

Hein, M. & Arena, S. (2010). *Foundations of College Chemistry, Alternate.* New York: John Wiley and Sons.

Howard, D., de Jonge, M., Lau, D., Hay, D., Varcoe-Cocks, M., Ryan, C., Kirkham, R., Moorhead, G., Paterson, D. & Thurrowgood, D. (2012). *Anal. Chem.* **84**, 3278–3286.

Hurtado, S., Garcia-León, M. & Garcia- Tenorio, R. (2004). *Nucl. Instrum. Methods Phys. Res. A*, **518**, 764–774.

Ivanchenko, V., Incerti, S., Allison, J., Bagulya, A., Brown, J., Champion, C., Elles, S., Francis, Z., Grichine, V., Ivantchenko, A. *et al.* (2014). *Proceedings of the International Conference on Supercomputing in Nuclear Applications and Monte Carlo.*

Kirkham, R. *et al.* (2010). *AIP Conf. Proc.* **1234**, 240.

Kirkpatrick, P. & Baez, A. V. (1948). *J. Opt. Soc. Am.* **38**, 766–773.

Lax, M., Louisell, W. H. & McKnight, W. B. (1975). *Phys. Rev. A*, **11**, 1365.

Lombi, E., De Jonge, M., Donner, E., Ryan, C. & Paterson, D. (2011). *Anal. Bioanal. Chem.* **400**, 1637–1644.

Mathieson, K., Passmore, M., Seller, P., Prydderch, M., O'Shea, V., Bates, R., Smith, K. & Rahman, M. (2002). *Nucl. Instrum. Methods Phys. Res. A*, **487**, 113–122.

McColl, G., James, S., Mayo, S., Howard, D., Ryan, C., Kirkham, R., Moorhead, G., Paterson, D., de Jonge, M. & Bush, A. (2012). *PloS One*, **7**, e32685.

Pratt, R., LaJohn, L., Florescu, V., Surić, T., Chatterjee, B. K. & Roy, S. (2010). *Radiat. Phys. Chem.* **79**, 124–131.

Pratt, R., LaJohn, L., Suric, T., Chatterjee, B. K. & Roy, S. (2007). *Nucl. Instrum. Methods Phys. Res. B*, **261**, 175–179.

Ryan, C. (2000). *Intl J. Imaging Syst. Technol.* **11**, 219–230.

Ryan, C., Cousens, D., Sie, S., Griffin, W., Suter, G. & Clayton, E. (1990). *Nucl. Instrum. Methods Phys. Res. B*, **47**, 55–71.

Ryan, C. & Jamieson, D. (1993). *Nucl. Instrum. Methods Phys. Res. B*, **77**, 203–214.

Ryan, C., Kirkham, R., Hough, R., Moorhead, G., Siddons, D., De Jonge, M., Paterson, D., De Geronimo, G., Howard, D. & Cleverley, J. (2010*a*). *Nucl. Instrum. Methods Phys. Res. A*, **619**, 37–43.

Ryan, C. *et al.* (2010*b*). *Nucl. Instrum. Methods Phys. Res. B*, **268**, 1899–1902.

Ryan, C. *et al.* (2014). *J. Phys. Conf. Ser.* **499**, 012002.

Saleh, B. & Teich, M. C. (1991). *Fundamentals of Photonics*, p. 3. New York: Wiley.

Siegman, A. E. (1986). *Lasers.* Mill Valley: University Science Books.

Sparks Jr, C., Borie, B. & Hastings, J. (1980). *Nucl. Instrum. Methods*, **172**, 237–242.

Starikov, A. & Wolf, E. (1982). *J. Opt. Soc. Am.* **72**, 923–928.

Veldhuizen, T. L. (1998). *Computing in Object-Oriented Parallel Environments*, pp. 223–230. Berlin: Springer.

Yang, B., Rivers, M., Schildkamp, W. & Eng, P. J. (1995). *Rev. Sci. Instrum.* **66**, 2278–2280.